

Landau levels and magneto-transport property of monolayer phosphorene

X. Y. Zhou,^{1,2} R. Zhang,¹ J. P. Sun,¹ Y. L. Zou,¹ D. Zhang,¹ W. K. Lou,¹ F. Cheng,⁴ G. H. Zhou,² F. Zhai,³ Kai Chang^{1*}

¹*SKLSM, Institute of Semiconductors, Chinese Academy of Sciences, P.O. Box 912, Beijing 100083, China.*

²*Department of Physics and Key Laboratory for Low-Dimensional Structures and Quantum Manipulation (Ministry of Education), Hunan Normal University, Changsha 410081, China.*

³*Department of Physics, Zhejiang Normal University, Jinhua 321004, China. and*

⁴*Department of Physics and Electronic Science, Changsha University of Science and Technology, Changsha 410004, China.*

We investigate theoretically the Landau levels (LLs) and magneto-transport properties of phosphorene under a perpendicular magnetic field within the framework of the effective $k\cdot p$ Hamiltonian and tight-binding (TB) model. At low field regime, we find that the LLs linearly depend both on the LL index n and magnetic field B , which is similar with that of conventional semiconductor two-dimensional electron gas. The Landau splittings of conduction and valence band are different and the wavefunctions corresponding to the LLs are strongly anisotropic due to the different anisotropic effective masses. An analytical expression for the LLs in low energy regime is obtained via solving the decoupled Hamiltonian, which agrees well with the numerical calculations. At high magnetic regime, a self-similar Hofstadter butterfly (HB) spectrum is obtained by using the TB model. The HB spectrum is consistent with the Landau level fan calculated from the effective $k\cdot p$ theory in a wide regime of magnetic fields. We find the LLs of phosphorene nanoribbon depend strongly on the ribbon orientation due to the anisotropic hopping parameters. The Hall and the longitudinal conductances (resistances) clearly reveal the structure of LLs.

PACS numbers: 73.50.-h, 72.80.Vp, 73.23.-b

I. INTRODUCTION

The group V element phosphorus can exist in several allotropes and black phosphorus (BP) is the most stable phase under normal conditions.¹ Recently, layered BP has attracted intensive attention because of its unique electronic properties and potential applications in nanoelectronics.²⁻⁸ In the bulk form, BP is a van der Waals-bonded layered material where each layer forms a puckered surface due to sp^3 hybridization.^{2,3} BP possesses a direct band gap 0.3 eV located at Z point.^{3,4} This direct gap moves to Γ point and increases to 1.5-2 eV when the thickness decreases from bulk to few layers and eventually monolayer via mechanical exfoliation.^{3,5,9} Hence, BP is an appealing candidate for tunable photodetection from the visible to the infrared part of the spectrum.¹⁰ Further, the field-effect-transistor (FET) based on few layer BP is found to have an on/off ratio of 10^5 and a carrier mobility at room temperature as high as 10^3 cm²/V·s,^{3,5,16} which make BP a favorable material for next generation electronics.

The low energy physics of monolayer BP (phosphorene) around Γ point can be well described by an anisotropic two band $k\cdot p$ model,² which agrees well with a tight binding (TB) model.¹¹ To date, various interesting properties for phosphorene have been predicted theoretically and verified experimentally, including those related to strain induced gap modification,² tunable optical properties,¹² layer controlled anisotropic excitons,¹³ quantum oscillations in few layers BP¹⁴⁻¹⁶ etc. However, the Landau levels (LLs) and magneto-transport (MT) properties of this unique anisotropic system remain unexplored.

In this work, we study the LL spectra and MT properties of phosphorene under a perpendicular magnetic field. By using an effective $k\cdot p$ Hamiltonian, we find that the LLs linearly depend both on energy index n and magnetic field B at low-field regime, which means the LLs in phosphorene are similar with that in conventional semiconductor two dimensional gases (2DEGs). Interestingly, owing to the anisotropic energy dispersions, i.e., the effective masses, the Landau splittings of conduction and valence band are different for a fixed magnetic field, and the wavefunctions corresponding to the LLs show strong anisotropic behavior. We obtain an analytical expression for the LLs in low energy regime via solving a decoupled Hamiltonian, which agrees well with the numerical data in low energy regime. At high-field regime, magneto-level spectrum, i.e., the Hofstadter butterfly (HB) spectrum, is obtained by using a tight binding (TB) model. We find that the results obtained by the effective $k\cdot p$ Hamiltonian and TB model agree with each other in weak magnetic field cases. Further, we find the LLs of phosphorene nanoribbon depend strongly on the ribbon orientation due to the anisotropic hopping parameters. In order to detect those interesting magneto energy spectra, we calculate MT properties of phosphorene within the framework of the linear response theory. By using Kubo formula, we find the Hall and the longitudinal conductances (resistances) clearly reveal the structure of LLs.

The paper is organized as follows. In Sec. II. A, we present the calculation method and obtain the effective Hamiltonian and LL spectra. In Sec. II. B, we calculate the Hall and longitudinal conductance by using Kubo formula. In Sec. III, we present the numerical results and discussions. Finally, we summarize our results in Sec. IV.

*To whom correspondence should be addressed: kchang@semi.ac.cn

II. MODEL AND HAMILTONIAN

A. Landau levels in monolayer phosphorene

In this subsection, we present the effective $\mathbf{k}\cdot\mathbf{p}$ and TB Hamiltonians and the calculation method about the LLs at low and high magnetic fields. In the top view of phosphorene, as shown in Figure 1(a), $\mathbf{a}_1=3.32 \text{ \AA}$ and $\mathbf{a}_2=4.48 \text{ \AA}$ are the primitive vectors, $a=2.22 \text{ \AA}$ and $\theta=96.76^\circ$ are the in-plane bond length and bond angle,¹¹ respectively. The unit cell of phosphorene contains four atoms (see the solid rectangle) with two phosphorus atoms in the lower layer and the other two atoms in the upper layer. Very recently, a tight binding (TB) model of phosphorene has been proposed and is given by¹¹

$$H = \sum_{\langle i,j \rangle} t_{ij} c_j^\dagger c_i, \quad (1)$$

where the summation runs over all the lattice sites of phosphorene, $c_j^\dagger(c_i)$ is the creation (annihilation) operator of electron on the site $j(i)$, and t_{ij} are the hopping parameters. It has been shown that five hopping links [see Fig. 1(a)] are enough to describe the electronic band structure of phosphorene.¹¹ The related hopping parameters are: $t_1=-1.22 \text{ eV}$, $t_2=3.665 \text{ eV}$, $t_3=-0.205 \text{ eV}$, $t_4=-0.105 \text{ eV}$, and $t_5=-0.055 \text{ eV}$.

Generally, the energy dispersion of phosphorene should be described by a four band model^{11,17} in the TB framework. However, it can be also expressed by a two-band model due to the C_{2h} point group invariance.¹⁷ In the two-band model, the unit cell contains two phosphorus atoms [see the dashed rectangle in Fig. 1(a)], where one is in the upper layer and the other in the lower layer. Expanding the TB model around Γ point with a coordinate rotation¹⁷ ($\tau_x \rightarrow \tau_z$, $\tau_y \rightarrow \tau_x$), one obtains the low energy $\mathbf{k}\cdot\mathbf{p}$ model for phosphorene, which reads

$$H = \begin{pmatrix} h_c & h_{cv} \\ h_{cv}^* & h_v \end{pmatrix} = \begin{pmatrix} E_c + \alpha k_x^2 + \beta k_y^2 & \gamma k_x \\ \gamma k_x & E_v - \lambda k_x^2 - \eta k_y^2 \end{pmatrix}, \quad (2)$$

where $E_c=0.34 \text{ eV}$ ($E_v=-1.18 \text{ eV}$) is the conduction (valence) band edge, $\gamma=-5.2305 \text{ eV}\cdot\text{\AA}$ describes the interband coupling between the conduction and valence band, parameters $\alpha, \beta, \lambda, \eta$ are related to the effective masses with $\alpha=\hbar^2/2m_{cx}$, $\beta=\hbar^2/2m_{cy}$, $\lambda=\hbar^2/2m_{vx}$, $\eta=\hbar^2/2m_{vy}$. Here $m_{cx}=0.793m_e$, $m_{cy}=0.848m_e$, $m_{vx}=1.363m_e$, $m_{vy}=1.142m_e$, and m_e is the free electron mass. The eigenvalue of this Hamiltonian is

$$E_{\pm} = \frac{1}{2} [h_c + h_v \pm \sqrt{(h_c - h_v)^2 + 4\gamma^2 k_x^2}], \quad (3)$$

where $+/-$ is for conduction/valence band, respectively. Similar with other low energy $\mathbf{k}\cdot\mathbf{p}$ models,^{2,12} the dispersion described by Eq. (3) is strongly anisotropic. The energy gap E_g is $E_c - E_v=1.52 \text{ eV}$, which is consistent with the first principle calculations (2 to 2.2 eV)¹³ and also in line with the recently measured optical gap⁵ 1.45 eV (the quasiparticle band gap minus the exciton binding energy). Figure 1 presents the dispersion of TB (the black solid line) and the $\mathbf{k}\cdot\mathbf{p}$ models (the red dashed line), from which we find they agree well with each

other in a quite wide energy regime. It seems the energy dispersion is linearly along $\Gamma-X$ direction [see Fig. 1(c)]. However, it is actually parabolic. In the long wave limit, we have $(h_c - h_v)^2 \approx E_g^2 \gg 4\gamma^2 k_x^2$. Hence, we can expand Eq. (3) and obtain the energy dispersion of conduction and valence band, which reads

$$E_+ \approx h_c + \frac{\gamma^2 k_x^2}{E_g}, E_- \approx h_v - \frac{\gamma^2 k_x^2}{E_g}, \quad (4)$$

From Eq. (4), one can easily find that the dispersion near Γ point is quadratic. Owing to the interband coupling, the effective masses along $\Gamma-X$ direction are modified as $m'_{cx}=\hbar^2/2(\alpha + \gamma^2/E_g)=0.167m_e$, $m'_{vx}=\hbar^2/2(\lambda + \gamma^2/E_g)=0.184m_e$. However, the effective masses along $\Gamma-Y$ remain unchanged with $m_{cy}=0.848m_e$, $m_{vy}=1.142m_e$.

When a perpendicular magnetic field $\mathbf{B}=(0,0,B)$ is applied, we define the creation and annihilation operators as

$$\hat{a} = \sqrt{\frac{m_{cy}\omega_c}{2\hbar}} (y - y_0 + i \frac{p_y}{m_{cy}\omega_c}), \\ \hat{a}^\dagger = \sqrt{\frac{m_{cy}\omega_c}{2\hbar}} (y - y_0 - i \frac{p_y}{m_{cy}\omega_c}), \quad (5)$$

where $\omega_c=eB/(m_{cx}m_{cy})^{\frac{1}{2}}$ is the frequency, $y_0=l_B^2 k_x$ is the cyclotron center, and $l_B=\sqrt{\hbar/eB}$ is the magnetic length. One finds Hamiltonian (2) turns to

$$H = \begin{pmatrix} h_c & 0 \\ 0 & h_v \end{pmatrix} + h_R + h_D, \quad (6)$$

with

$$h_R = \hbar\omega_\gamma \begin{pmatrix} 0 & \hat{a} \\ \hat{a}^\dagger & 0 \end{pmatrix}, h_D = \hbar\omega_\gamma \begin{pmatrix} 0 & \hat{a}^\dagger \\ \hat{a} & 0 \end{pmatrix}, \\ h_c = E_c + (\hat{a}^\dagger \hat{a} + 1/2)\hbar\omega_c, \\ h_v = E_v - (\hat{a}^\dagger \hat{a} + 1/2)\hbar\omega_v - (\hat{a}^2 + \hat{a}^{\dagger 2})\hbar\omega', \quad (7)$$

where $\omega_\gamma=\gamma/\sqrt{2}\hbar l_B \alpha_{yx}$, $\omega_v=(r_x+r_y)\omega_c$, $\omega'=(r_x-r_y)\omega_c/2$, with $\alpha_{yx}=(m_{cy}/m_{cx})^{\frac{1}{2}}$, $r_x=m_{cx}/2m_{vx}$ and $r_y=m_{cy}/2m_{vy}$. Interestingly, the second (third) term in Eq. (6) looks like the Rashba (Dresselhaus) spin-orbit interaction in conventional semiconductor 2DEG.²¹ In order to understand how the non-diagonal element h_R and h_D couple the Landau levels (LLs) in conduction and valence band, we first simplify the Hamiltonian by ignoring the third term in h_v [see Eq. (7)] since it is a second-order perturbation. It will be included in numerical calculation. In this approximation, we see that the term h_R couples the LL $\phi_n|c\rangle$ with $\phi_{n+1}|v\rangle$, while h_D couples $\phi_{n+1}|c\rangle$ with $\phi_n|v\rangle$, where $|c\rangle = \begin{pmatrix} 1 \\ 0 \end{pmatrix}$, $|v\rangle = \begin{pmatrix} 0 \\ 1 \end{pmatrix}$, $\{\phi_n\}$ are wave functions of the harmonic oscillator corresponding to h_c .

Taking Landau gauge $\mathbf{A}=(-By,0,0)$, when only the term h_R exists, we obtain $E_{n,\pm}^R=(E_{nc} + E_{nv} \pm \Omega_n^R)/2$, $\psi_{nk_x,\pm}^R=e^{ik_x x}/\sqrt{L_x}\varphi_{nk_x,\pm}^R$ ($n=1,2,\dots$), where

$$\varphi_{nk_x,+}^R = \sin \frac{\vartheta_n}{2} \phi_{n-1}|c\rangle + \cos \frac{\vartheta_n}{2} \phi_n|v\rangle, \\ \varphi_{nk_x,-}^R = \cos \frac{\vartheta_n}{2} \phi_{n-1}|c\rangle - \sin \frac{\vartheta_n}{2} \phi_n|v\rangle. \quad (8)$$

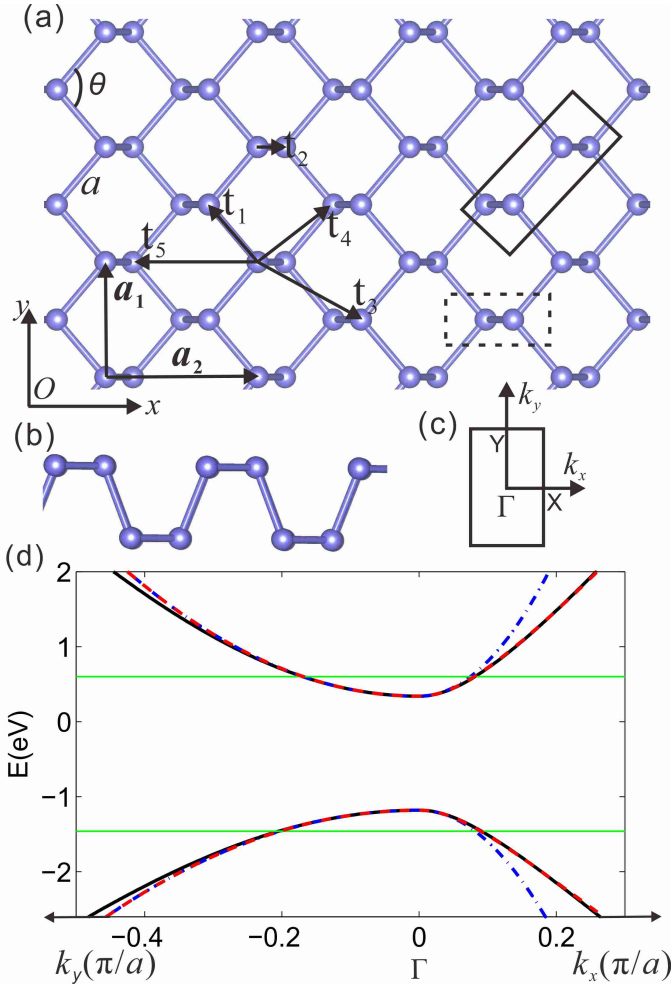


FIG. 1: (Color online) (a) The top view of phosphorene, $a=2.22$ Å ($\theta=96.76^\circ$) is the in plane bond length (angel), \mathbf{a}_1 (3.32 Å) and \mathbf{a}_2 (4.48 Å) the primitive vectors, t_i ($i = 1, 2, 3, 4, 5$) the five hopping links for TB model. (b) The side view of phosphorene. (c) The first Brillouin zone of phosphorene, the black solid and red dashed lines, represent the results obtained from the TB and low energy $\mathbf{k}\cdot\mathbf{p}$ models, respectively. The blue dash-dotted lines represent the results from the decoupled Hamiltonian (13) and the green solid line illustrates the energy regime where three Hamiltonians agree well with each other.

Here Ω_n^R and ϑ_n are defined from $\Omega_n^R \cos \vartheta_n = E_{nc} - E_{nv}$, $\Omega_n^R \sin \vartheta_n = 2\sqrt{n}\hbar\omega_\gamma$. The h_R induces the coupling of the LL's, which is schematically shown in Fig. 2(a). We see that both $\varphi_{nk_x+}^R$ and $\varphi_{nk_x-}^R$ come from $\phi_{n-1}|c\rangle$ and $\phi_n|v\rangle$. A particular eigenstate is the lowest LL in valence band ($\phi_0|v\rangle$), which is independent of h_R . Meanwhile, when only h_D exists, we obtain $E_{n,\pm}^D = E_{n,\pm}^R$, $\psi_{nk_x\pm}^D = e^{ik_x x} / \sqrt{L_x} \varphi_{nk_x\pm}^D$ ($n=1, 2, \dots$), where

$$\begin{aligned} \varphi_{nk_x+}^D &= \sin \frac{\vartheta_n}{2} \phi_n|c\rangle + \cos \frac{\vartheta_n}{2} \phi_{n-1}|v\rangle, \\ \varphi_{nk_x-}^D &= \cos \frac{\vartheta_n}{2} \phi_n|c\rangle - \sin \frac{\vartheta_n}{2} \phi_{n-1}|v\rangle. \end{aligned} \quad (9)$$

The h_D induces the coupling of the LL's as schematically shown in Fig. 2(b). We see that both $\varphi_{nk_x+}^D$ and $\varphi_{nk_x-}^D$ come

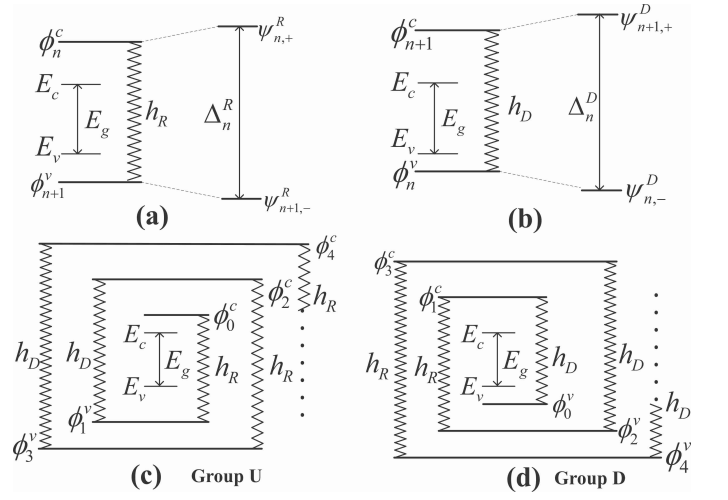


FIG. 2: Schematic illustration of the inter-LL coupling induced by (a) h_R with $\Delta_n^R = E_{n,+}^R - E_{n+1,-}^R$ and (b) h_D with $\Delta_n^D = E_{n+1,+}^D - E_{n,-}^D$; while (c)/(d) represents coupled LL in group U/D.

from $\phi_n|c\rangle$ and $\phi_{n-1}|v\rangle$. A particular eigenstate is the lowest LL in conduction band ($\phi_0|c\rangle$), which is independent of h_D . Therefore, when both h_R and h_D exist, the LLs are coupled into the following two groups

$$\phi_0|c\rangle \xleftrightarrow{h_R} \phi_1|v\rangle \xleftrightarrow{h_D} \phi_2|c\rangle \xleftrightarrow{h_R} \phi_3|v\rangle \xleftrightarrow{h_D} \dots \text{(group } U\text{)} \quad (10)$$

and

$$\phi_0|v\rangle \xleftrightarrow{h_D} \phi_1|c\rangle \xleftrightarrow{h_R} \phi_2|v\rangle \xleftrightarrow{h_D} \phi_3|c\rangle \xleftrightarrow{h_R} \dots \text{(group } D\text{)} \quad (11)$$

The two groups are schematically illustrated in Figs. 2(c) and 2(d). The eigenvalues and eigenvectors can be evaluated numerically by taking the eigenvectors of h_c in Eq. (7) as basis functions. In this basis, the wavefunction of the system can be expressed as

$$\psi(x, y) = \frac{e^{ik_x x}}{\sqrt{L_x}} \sum_{m=0}^M \begin{pmatrix} c_m \\ d_m \end{pmatrix} \phi_m[\kappa(y - y_0)], \quad (12)$$

where $\kappa = \sqrt{m c_y \omega_c / \hbar}$, $\phi_m(y) = e^{-\gamma^2/2} H_m(y) / (\sqrt{\pi} 2^m m!)^{1/2}$ is the harmonic oscillator wave functions. Then, we can diagonalize the Hamiltonian numerically in a truncated Hilbert space and obtain the eigenvalues as well as the eigenvectors.

From the Hamiltonian (2), the LLs can be solved analytically in low energy regime. Although the dispersion is dominated by the off-diagonal element, we can decouple the conduction and valence band in low energy regime due to the large band gap (1.52 eV), i.e., the weak interband coupling. The role of the off-diagonal elements can be taken into account perturbatively. The decoupled Hamiltonian reads

$$H = \begin{pmatrix} h'_c & 0 \\ 0 & h'_v \end{pmatrix} = \begin{pmatrix} E_c + \alpha' k_x^2 + \beta k_y^2 & 0 \\ 0 & E_v - \lambda' k_x^2 - \eta k_y^2 \end{pmatrix}, \quad (13)$$

where $\alpha' = \alpha + \gamma^2 / E_g$, $\lambda' = \lambda + \gamma^2 / E_g$. The dispersion of this Hamiltonian is presented by the blue dash-dotted lines in Fig.

1(d). We see that in the energy regime about 300 meV (see the green solid line) with respect to the band edges the decoupled Hamiltonian agrees well with the TB and the $\mathbf{k}\cdot\mathbf{p}$ model. The LL of this Hamiltonian is

$$E_{n,c} = E_c + (n + \frac{1}{2})\hbar\omega'_c, \quad E_{n,v} = E_v - (n + \frac{1}{2})\hbar\omega'_v, \quad (14)$$

where $n=0,1,2,3,\dots$, represents the LL index, the effective cyclotron frequency $\omega'_c = eB/\sqrt{(m'_{cx}m_{cy})} = 2.657\omega_e$ and $\omega'_v = eB/\sqrt{(m'_{vx}m_{vy})} = 2.182\omega_e$ with $\omega_e = eB/m_e$. Note, unlike the anisotropic zero field dispersion, this LL spectrum is independent on the in-plane wavevectors. However, the corresponding eigenvectors are anisotropic due to different effective masses along Γ - X and Γ - Y direction. In Landau gauge $\mathbf{A}=(-By, 0, 0)$, the eigenvectors are

$$\psi_{n,+}(x, y) = \frac{e^{ik_x x}}{\sqrt{L_x}} \begin{pmatrix} \phi_n(y_c) \\ 0 \end{pmatrix}, \quad \psi_{n,-}(x, y) = \frac{e^{ik_x x}}{\sqrt{L_x}} \begin{pmatrix} 0 \\ \phi_n(y_v) \end{pmatrix}, \quad (15)$$

where $y_{c/v} = \kappa_{c/v}(y - y_0)$ with $\kappa_i = \sqrt{m_{iy}\omega'_i/\hbar}$ ($i=c, v$). While in Landau gauge $\mathbf{A}=(0, Bx, 0)$, the eigenvectors are

$$\psi_{n,+}(x, y) = \frac{e^{ik_y y}}{\sqrt{L_y}} \begin{pmatrix} \phi_n(x_c) \\ 0 \end{pmatrix}, \quad \psi_{n,-}(x, y) = \frac{e^{ik_y y}}{\sqrt{L_y}} \begin{pmatrix} 0 \\ \phi_n(x_v) \end{pmatrix}, \quad (16)$$

where $x_{c/v} = \kappa'_{c/v}(x - x_0)$, with $\kappa'_i = \sqrt{m'_{ix}\omega'_i/\hbar}$ ($i=c, v$). Obviously, the corresponding eigenvectors are anisotropic due to different effective masses according to Eqs. (15) and (16). Further, we will see this anisotropy more clearly in symmetry gauge. The wavefunctions in symmetry gauge are given by

$$\psi_{n,m}(x, y) = A_{n,m} e^{-|Z|^2/2} Z^{|m|} L_n^{|m|}(|Z|^2), \quad (17)$$

where $Z=X+iY$, $X=(x+\delta y)/\sqrt{2\delta}l_B$, $Y=(x-\delta y)/\sqrt{2\delta}l_B$, and $\delta = \sqrt{m_{cy}/m_{cx}} (\sqrt{m_{vy}/m_{vx}})$ for conduction (valence) band, and $A_{n,m} = (-1)^n \sqrt{n!/(n-m)!} \pi$ is the normalization constant, $L_n^m(x)$ is the Laguerre polynomials.

In the TB framework, when the phosphorene sample subjected to a perpendicular magnetic field, a Peierls phase should be added to the hopping parameter, which reads

$$H = \sum_{\langle i,j \rangle} t_{ij} e^{i2\pi\phi_{ij}} c_j^\dagger c_i, \quad (18)$$

where $\phi_{ij} = \frac{e}{\hbar} \int_{r_i}^{r_j} \mathbf{A} \cdot d\mathbf{l}$ is the Peierls phase. It was first shown by Hofstadter¹⁸ that the energy spectrum in this case depends on a rational dimensionless parameter p/q , where q is a prime number and p runs from 1 to q . This dimensionless parameter is the ratio of magnetic flux through one unit cell ($\Phi = BS$) to the magnetic flux quantum ($\Phi_0 = h/e = 4.14 \times 10^{-15} \text{T m}^2$), where S is the area of a unit cell. The energies plotted as a function of Φ/Φ_0 form a beautiful Hofstadter Butterfly (HB) spectrum. By using Eq. (17), one will arrive the the Haper's equation and find it is periodic in $2q$.¹⁹ The HB spectrum is obtained numerically by getting the eigenvalues of a matrix with dimension of $4q \times 4q$ at each \mathbf{k} point in the magnetic Brillouin zone. A sufficiently large q is needed if one wants to compare this HB spectrum with the results obtained from the low energy $\mathbf{k}\cdot\mathbf{p}$ model due to the large magnetic flux quanta.

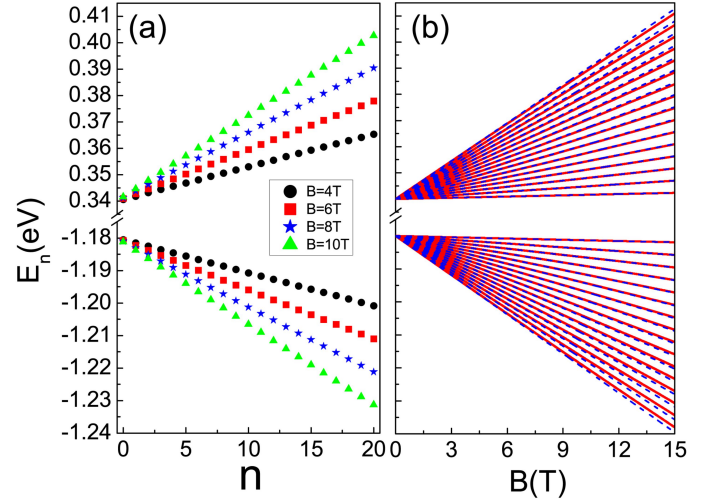


FIG. 3: (Color online) Landau levels (E_n in units of eV) versus (a) Landau energy index n with different magnetic field, and (b) magnetic field B for the first ten low LLs. The number of the basis function used is 200 to get convergent results. The red solid lines denote the numerical data and the blue dashed lines represent the analytical expression in Eq. (14).

B. Magneto-transport properties

In order to detect the calculated magneto energy spectrum, we study the magneto-transport properties of phosphorene in this subsection. In the presence of a perpendicular magnetic field, there are two contributions to magnetoconductance:²⁰ the Hall and collisional conductance. The former is from the non-diagonal contribution and the later from the localized states which contribute to the Shubnikov-de Haas (SdH) oscillation. In order to calculate the electrical conductance in the presence of a magnetic field, we follow the formulation of the general Liouville equation.²⁰ This formulation has been employed successfully in electron transport for conventional semiconductor 2DEG,^{20,21} and more recently in graphene²² and MoS_2 .²³

Within linear response theory, the Hall conductance in Kubo-Greenwood formula reads²⁰

$$\sigma_{\mu\nu}^{\text{nd}} = \frac{i\hbar e^2}{S_0} \sum_{\zeta \neq \zeta'} \frac{[f(E_\zeta) - f(E_{\zeta'})] \langle \zeta | v_\mu | \zeta' \rangle \langle \zeta' | v_\nu | \zeta \rangle}{(E_\zeta - E_{\zeta'})(E_\zeta - E_{\zeta'} + i\Gamma_\zeta)}, \quad (19)$$

where $\mu, \nu = x, y$, $S_0 = L_x L_y$ is the phosphorene sample area, with the size L_x (L_y) in x (y)-direction, $|\zeta\rangle = |s, n, k_x\rangle$ the single electron state in Eq. (15) as we are interested in the low energy transport, $f(E_\zeta) = [e^{(E_\zeta - E_F)/k_B T} + 1]^{-1}$ the Fermi-Dirac distribution function with Boltzman constant k_B and temperature T , $v_\mu = \partial H / \partial p_\mu$ the component of group velocity. The sum runs over all states $|\zeta\rangle = |s, n, k_x\rangle$ and $|\zeta'\rangle = |s', n', k'_x\rangle$ with $\zeta \neq \zeta'$. The infinitesimal quantity Γ_ζ accounts for the finite broadening of the LLs, which is assumed approximately the same for all states²². In our work, we take $\Gamma_\zeta = 0$ in order to obtain a transparent result for Hall conductance. The Hall conductance

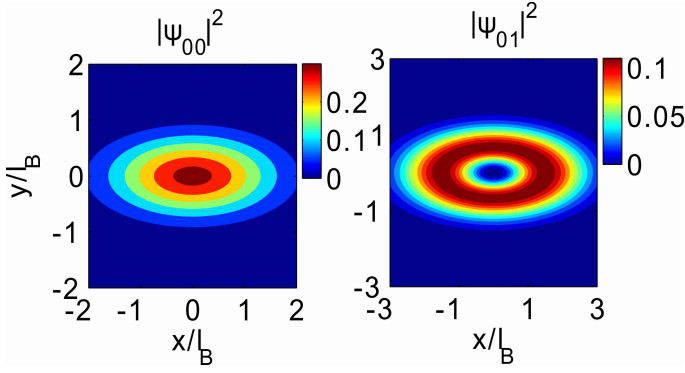


FIG. 4: (Color online) Contour plot of the spatial density distributions of the first two LLs in conduction band in symmetry gauge.

is

$$\sigma_{xy} = g_s \frac{e^2}{h} \sum_{n=0, s=\pm} (n+1) [f(E_{n,s}) - f(E_{n+1,s})], \quad (20)$$

where $g_s=2$ for the spin degree of freedom. At low temperature, the Hall conductance turns

$$\sigma_{xy} = j g_s \frac{e^2}{h}, \quad (j = 0, 1, 2, 3 \dots) \quad (21)$$

where j is the filling factor. This result is the same as that for a conventional semiconductor 2DEG^{20,21} since the zero field dispersion in low energy regime is quadratic [see Eq. (4)].

To obtain the longitudinal conductance, we assume that electrons are elastically scattered by randomly distributed charged impurities, as this type of scattering is dominant at low temperatures. The longitudinal conductance in Kubo-Greenwood formula is given by²²

$$\sigma_{xx}^{\text{col}} = \frac{\beta e^2}{2S_0} \sum_{\zeta, \zeta'} f(E_{\zeta}) [1 - f(E_{\zeta'})] W_{\zeta\zeta'}(E_{\zeta}, E_{\zeta'}) (y_{\zeta} - y_{\zeta'})^2 \quad (22)$$

where $W_{\zeta\zeta'}$ is the scattering rate between one-electron states $|\zeta\rangle$ and $|\zeta'\rangle$. Conduction occurs via transitions through spatially separated states from y_{ζ} to $y_{\zeta'}$, where $y_{\zeta} = \langle \zeta | y | \zeta \rangle$ is the expectation value of y coordinate. This means that the longitudinal conductance arises from the migration of the cyclotron orbit because of scattering by charged impurities. The scattering rate $W_{\zeta\zeta'}$ is

$$W_{\zeta\zeta'} = \frac{2\pi n_i}{\hbar S_0} \sum_q |U_q|^2 |F_{\zeta, \zeta'}(u)|^2 \delta(E_{\zeta} - E_{\zeta'}) \delta_{k_x, k'_x + q_x}, \quad (23)$$

where $q = \sqrt{q_x^2 + q_y^2}$, $u = l_B^2 q^2 / 2$, n_i is the impurity density, $U_q = U_0 / \sqrt{q^2 + k_s^2}$ the Fourier transform of the screened impurity potential $U(r) = U_0 e^{-k_s r} / r$ with $U_0 = e^2 / 4\pi\epsilon_0\epsilon_r$, k_s the screening wavevector, ϵ_r the dielectric constant and ϵ_0 the dielectric permittivity. Furthermore, if the impurity potential is strongly short ranged (of the Dirac δ -type function), one may use the approximation $k_s \gg q$ and $U_q \approx U_0 / k_s$. As the collision

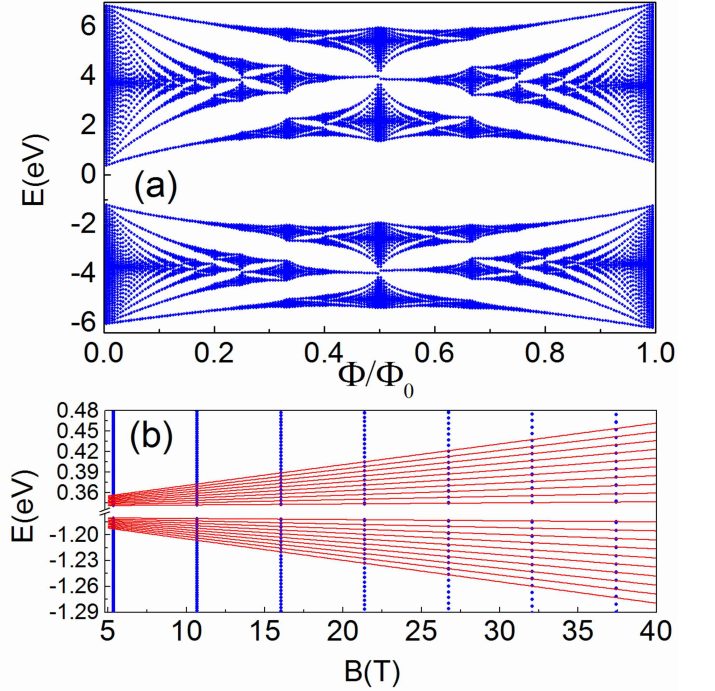


FIG. 5: (Color online) (a) Hofstadter butterfly (HB) spectrum of phosphorene with $q=199$ and hopping parameters $t_1=-1.22$ eV, $t_2=3.665$ eV, $t_3=-0.205$ eV, $t_4=-0.105$ eV and $t_5=-0.055$ eV. (b) Landau levels obtained from the TB model, i.e., the HB spectrum (the blue dots) and the $k \cdot p$ model (the red solid line) as a function of magnetic field at low field regime with $q=10007$.

is elastic and the eigenvalue is independent on k_x , only the transitions $n \rightarrow n$ are allowed. The longitudinal conductance is

$$\sigma_{xx} = g_s \frac{e^2}{h} \frac{n_i U_0^2}{k_B T \hbar \omega_s k_s^2 l_B^2} \sum_{n=0, s=\pm} (2n+1) f(E_{n,s}) [1 - f(E_{n,s})] \quad (24)$$

Moreover, one can obtain the Hall resistance and the longitudinal one with the conductances (σ_{xy} and σ_{xx}) via expressions of $\rho_{xy} = \sigma_{xy} / S$ and $\rho_{xx} = \sigma_{xx} / S$, where $S = \sigma_{xx} \sigma_{yy} - \sigma_{xy} \sigma_{yx} \approx \sigma_{xy}^2 = n_e^2 e^2 / B^2$,²⁰⁻²² and n_e is the electron concentration. For a fixed Fermi energy (E_f), n_e is given by $n_e = \int_0^{E_f} D(E) dE$, where $D(E) = \frac{g_s}{\pi l_B^2} \sum_n \delta(E - E_n)$ is the density of states. Note, no matter which wavefunction [Eq. (15) or (16)] is used in the calculation, one will obtain the same results as the conductances are gauge independent.

III. NUMERICAL EXAMPLES AND DISCUSSION

Next, we show the numerical results with experimental reachable parameters, i.e., temperature $T=1$ K, impurity concentration $n_i=2 \times 10^8$ cm⁻², screen potential vector $k_s=5 \times 10^7$ m⁻¹, and dielectric constant²⁴ $\epsilon_r=10.2$.

Figure 3 presents the LLs versus (a) LL index n with different magnetic fields and (b) magnetic field B . The red solid

lines denote the numerical data and the blue dashed lines represent the analytical results in Eq. (14) for the low energy LLs. The number of basis function used in the calculation is 200 to get convergent numerical results. As shown in figure 3(b), we find the analytical LLs (the blue dashed lines) are in good agreement with the numerical results (the red solid lines), which means the decouple Hamiltonian (13) is a good approximation in low energy regime. However, the Landau splittings of conduction and valence band are different for a fixed magnetic field [see Eq. (14)] due to the different anisotropic effective masses at zero field. Further, the Landau energies linearly depend both on LL index n [see Fig. 2(a)] and magnetic field B [see Fig. 2(b)], which is similar with that of conventional semiconductor 2DEGs since the zero field dispersion is quadratic [see Eq. (4)]. Meanwhile, we find the LLs are equally spaced which can also be seen clearly in Eq. (14).

Arising from the strongly anisotropic band structure at zero field, the wavefunctions are anisotropic. Figure 4 presents the contour plot of spatial density distributions (SDDs) corresponding to the first two LLs in conduction band. As plotted in Fig. 4, unlike the isotropic case, we find the SDDs for the first two LL are ellipses, which show strong anisotropy. The decay length of the SDDs along x direction is larger than that along y direction as the effective masses along Γ - X direction is smaller than that in Γ - Y direction [see Eq. (4)] in conduction band. The same conclusion can be drawn for SDDs corresponding to LLs in valence band.

Adopting the TB model, we plot the Hofstadter Butterfly (HB) spectrum as a function of Φ/Φ_0 (magnetic field B) with $q=199$ in Fig. 5(a). As shown in Fig. 5(a), we find two gapped self-similar HB spectrum coming from the conduction and valence orbitals, respectively. Moreover, the LL energies linearly depend on magnetic field B at low field region, which is in line with the results obtained from the $\mathbf{k}\cdot\mathbf{p}$ model [see Eq. (14)]. The band width of the HB spectrum in conduction and valence band is different because of the different band widths at zero field. Figure 5(b) depicts the magneto-levels i.e., the HB spectrum (the blue dots) and the LLs (the red solid lines) calculated from the $\mathbf{k}\cdot\mathbf{p}$ theory as a function of magnetic field at low field regime with $q=10007$. As shown in the figure, we find they agree well with each other in wide regime of magnetic fields.

Figure 6 shows the energy spectra of a zigzag-edged PNR (ZPNR) with and without an external magnetic field. When a strong magnetic field $B=30$ T is applied perpendicular to the ZPNR, one can clearly see the LLs. While for an armchair-edged phosphorene nanoribbon (APNR) with the same width, the LLs show different energy spacing with that in the ZPNR for the higher LLs. Comparing the energy spectra of the ZPNR and APNR, an important difference between them is that there is a topological quasi-flat band located in the bulk gap of the ZPNR¹⁷. There are two kinds of edge states in ZPNRs. The one is the edge states arising from the LLs in ZPNR, the other come from the topological quasi-flat band. The degeneracy of the topological quasi-flat band lifts under the influence of the magnetic field. However, since the topological quasi-flat band are mainly localized near the edges, and

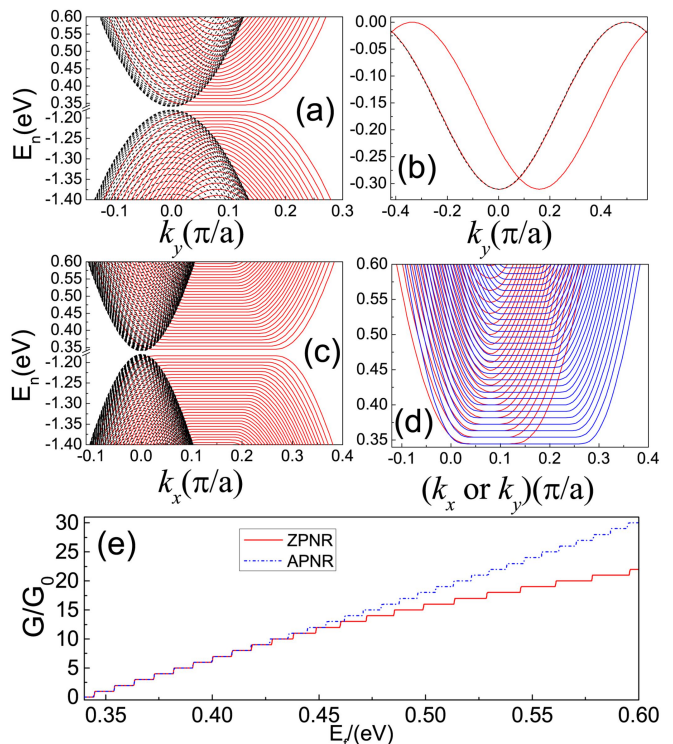


FIG. 6: (Color online) (a) LLs in a ZPNR with width $w=66.4$ nm, the red solid and black dashed lines represent the energy spectra with and without external magnetic fields, respectively; $B=30$ T ($l_B=4.67$ nm); (b) The same for (a), but for topological flat band located in the bulk gap. (c) LLs in APNR with the same parameters used in (a). (d) LLs in ZPNR (red solid lines) and APNR (blue solid lines) to show clearly the anisotropic feature of the LLs; (e) Conductance (in unit of $G_0=2e^2/h$) as a function of Fermi energy for ZPNR (red solid line) and APNR (blue dash-dotted line) corresponding to (d).

the decay length (~ 1.2 nm) is less than the magnetic length ($l_B=25.6\text{nm}/\sqrt{B}=4.67$ nm), the edge states arising from the topological quasi-flat band are almost independent of magnetic fields, i.e., no Landau quantization (see Fig. 6(b)). The LLs of PNRs depend strongly on the ribbon orientation due to the anisotropic band structure of bulk phosphorene (see Fig. 6(d)). This anisotropy of the LLs can be observed in the conductance (see Fig. 6(e)) as a function of Fermi energy (E_f) for ZPNR (red solid line) and APNR (blue dash-dotted line).

Figure 7 shows (a) the Hall (σ_{xy}) and (b) the longitudinal conductances (σ_{xx}) as a function of Fermi energy (E_f) for two different magnetic fields $B=4$ T and 8 T, respectively. As plotted in Fig. 7(a), we find that Hall conductance is strictly quantized due to the quantized LLs. It increases one by one in the unit of $G_0=2e^2/h$ with the increasing of Fermi energy since the LLs are filled one by one. Therefore, we observe the integer Hall plateaus at $0, \pm 2, \pm 4, \pm 6, \dots$ in Hall conductance. This is similar with that in conventional semiconductor 2DEG.²¹ Moreover, the Hall conductance reveals the LLs clearly since the transitions of the plateaus happen to be the energy value of LLs [see Fig. 3(a)]. Further, for a fixed magnetic field, the width of the plateaus is equal since the

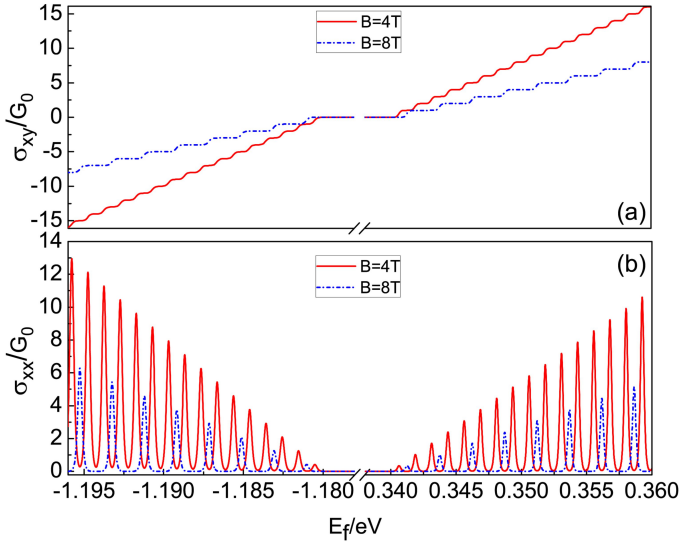


FIG. 7: (Color online)(a) Hall conductance σ_{xy} (in unit of $G_0 = 2e^2/h$) and (b) longitudinal conductance versus Fermi energy E_f (in unit of eV) with different magnetic fields. The parameters used are: temperature $T=1$ K, impurity concentration $n_i=2\times 10^8$ cm^{-2} , screen potential vector $k_s=5\times 10^7$ m^{-1} , Boltzman constant $k_B=1.38\times 10^{23}$ J/K, and dielectric constant $\epsilon_r=10.2$.

LL spacings of two adjacent LLs are equal according to Eq. (14). As depicted in Fig. 7(b), the longitudinal conductance shows that (i) pronounced peaks appear when the Fermi energy coincides with the LLs, and (ii) a well splitting SdH oscillation can be observed, which corresponds to the LLs [see Fig. 3(a)]. Meanwhile, the amplitude of longitudinal conductance increases with the increasing of the Fermi energy because of the larger scattering rate of LLs with higher index. Further, for a given magnetic field, the amplitude of longitudinal conductance for electrons and holes are slightly different due to distinct Landau splittings in conduction and valence bands [see Eq. (14)]. Moreover, the intervals between the peaks are equal since the LLs are equally spaced according to Eq. (14).

Finally, in Figure 8 we plot the Fermi energy spectra and resistances as a function of magnetic field for a fixed electron concentration $n_e=1.45\times 10^{12}$ cm^{-2} . Generally, the Hall (ρ_{xy}) and the longitudinal resistances (ρ_{xx}) can be detected directly via Hall measurement.^{3,14} As shown in figure 8(b), at low magnetic field, the Hall resistance linearly depend on the magnetic field and the longitudinal one is a constant. However, at the high magnetic field regime, the Hall resistance is strictly quantized with Hall plateaus due to Landau quantization. It increases (in unit of $\rho_0=h/e^2$) one by one with increasing magnetic field since the LLs leak out of the Fermi level one by one [see Fig. 8(a)]. This is also reflected in the transitions of filling factor [see Fig. 8(b)]. Therefore, we observe plateaus at $1/8, 1/10, 1/12, 1/14, \dots$, in Hall resistance corresponding to filling factor $j=4, 5, 6, 7, \dots$, with the decreasing of magnetic field. Meanwhile, we find a clear SdH oscillation in longitudinal resistance. The amplitude of longitudinal resistance increases with the magnetic field since it

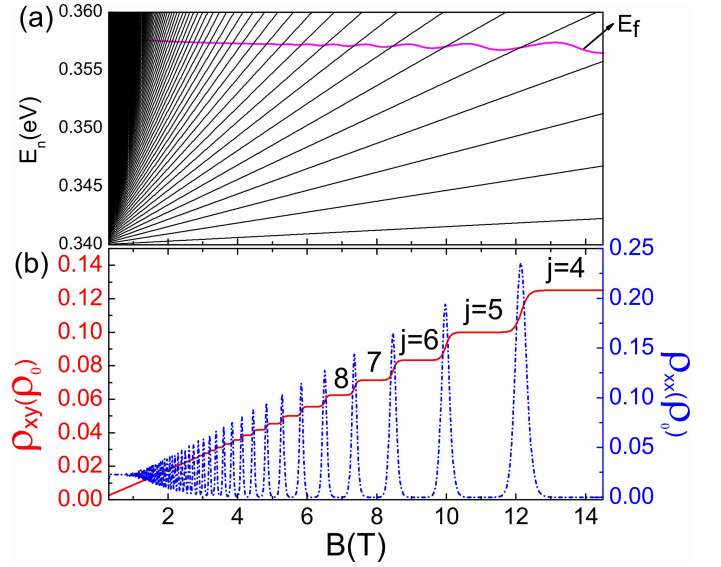


FIG. 8: (Color online) (a) Electron Fermi energy as a function of magnetic field for a fixed electron concentration $n_e=1.45\times 10^{12}$ cm^{-2} , (b) Hall resistance (the red solid line) and magneto longitudinal resistance (the blue dash-dotted line) corresponding to (a), the resistance unit ρ_0 is h/e^2 . The other parameters used are the same as Fig. 7.

is proportional to B^2 . However, this oscillation is quenched in low magnetic field due to tiny LL splittings in weak field cases.

IV. SUMMARY

We studied theoretically the Landau levels and magneto-transport properties of phosphorene under a perpendicular magnetic field within the framework of an effective $k\cdot p$ Hamiltonian and TB model. In the low field regime, we found that the LLs linearly depend both on the LL index n and magnetic field B , which is similar with that of conventional semiconductor two-dimensional electron gas. For a fixed magnetic field, the Landau splittings of conduction and valence band are different and the wavefunctions corresponding to the LLs show strong anisotropic behavior due to the anisotropic effective masses. We obtained an analytical expression for the LLs in low energy regime via solving a decoupled Hamiltonian. This analytical solution agrees well with the numerical results. At high magnetic regime, a self-similar Hofstadter butterfly (HB) spectrum was obtained by using the TB model. The HB spectrum is in good agreement with the LLs calculated from the effective $k\cdot p$ theory in a wide regime of magnetic fields.

Further, we found the LLs of phosphorene nanoribbons (PNRs) depend strongly on the ribbon orientation due to the anisotropic hopping parameters. There are two kinds of edge states in ZPNRs under a perpendicular magnetic field. The one is the edge states arising from the LLs, the other comes from the topological flat band. The second edge states are al-

most independent of magnetic fields because their decaying length is less than the magnetic length l_B . Moreover, the Hall and the longitudinal conductances (resistances) clearly reveal the structure of LLs in phosphorene sheet.

Our conclusions about the LL spectrum in phosphorene can be also applied to multilayer BPs since the $k \cdot p$ Hamiltonians for the multilayer ones are similar with that for phosphorene. A very recent paper²⁵ demonstrates that the low energy LLs in bulk phosphorus also depend linearly both on the LL index n and magnetic field B . Meanwhile, this result has been verified in several recent magneto transport experiments¹⁴⁻¹⁶.

Our results have been employed to illustrate the absence of non-trivial Berrys phase of LLs in multilayer BPs¹⁴.

Acknowledgments

This work was supported by the NSFC Grants No. 11434010 and the grant No. 2011CB922204 from the MOST of China, and NSFC Grants No. 11174252, and No. 11274108.

-
- ¹ T. Nishii, Y. Maruyama, T. Inabe, I. Shirovani, *Synth. Met.* **18**, 559 (1987).
- ² A. S. Rodin, A. Carvalho, and A. H. Castro Neto, *Phys. Rev. Lett.* **112**, 176801 (2014).
- ³ Likai Li, Yijun Yu, Guojun Ye, Qingqin Ge, Xuedong Ou, Hua Wu, Donglai Feng, Xian Hui Chen, and Yuanbo Zhang, *Nat. Nanotechnol.* **9**, 372 (2014).
- ⁴ C. Q. Han, M. Y. Yao, X. X. Bai, Lin Miao, Fengfeng Zhu, D. D. Guan, Shun Wang, C. L. Gao, Canhua Liu, Dong Qian, Y. Liu, and Jin-feng Jia, *Phys. Rev. B* **90**, 085101 (2014).
- ⁵ Han Liu, Adam T. Neal, Zhen Zhu, Zhe Luo, Xianfan Xu, David Tománek, and Peide D. Ye, *Acs Nano*. **8**, 4033 (2014).
- ⁶ H. O. Churchill and P. Jarillo-Herrero, *Nat. Nanotechnol.* **9**, 330 (2014).
- ⁷ E. S. Reich, *Nature* **506**, 19 (2014).
- ⁸ Andres Castellanos-Gomez, Leonardo Vicarelli, Elsa Prada, Joshua O Island, K L Narasimha-Acharya, Sofya I Blanter, Dirk J Groenendijk, Michele Buscema, Gary A Steele, J V Alvarez, Henny W Zandbergen, J J Palacios and Herre S J van der Zant, *2D Mater.* **1**, 025001 (2014).
- ⁹ Wanglin Lu, Haiyan Nan, Jinhua Hong, Yuming Chen, Chen Zhu, Zheng Liang, Xiangyang Ma, Zhenhua Ni, Chuanhong Jin, and Ze Zhang, *Nano. Res.* **7** 853 (2014).
- ¹⁰ Michele Buscema, Dirk J. Groenendijk, Sofya I. Blanter, Gary A. Steele, Herre S. J. van der Zant, and Andres Castellanos-Gomez, *Nano. Lett.* **14**, 3347 (2014).
- ¹¹ A. N. Rudenko and M. I. Katsnelson, *Phys. Rev. B* **89**, 201408(R) (2014).
- ¹² Tony Low, A. S. Rodin, A. Carvalho, Yongjin Jiang, Han Wang, Fengnian Xia, and A. H. Castro Neto, *Phys. Rev. B* **90**, 075434 (2014).
- ¹³ Vy Tran, Ryan Soklaski, Yufeng Liang, and Li Yang, *Phys. Rev. B* **89**, 235319 (2014).
- ¹⁴ Likai Li, Guo Jun Ye, Vy Tran, Ruixiang Fei, Guorui Chen, Huichao Wang, Jian Wang, Kenji Watanabe, Takashi Taniguchi, Li Yang, Xian Hui Chen and Yuanbo Zhang, arXiv:1411.6572.
- ¹⁵ Xiaolong Chen, Yingying Wu, Zefei Wu, Shuigang Xu, Lin Wang, Yu Han, Weiguang Ye, Tianyi Han, Yuheng He, Yuan Cai, Ning Wang, arXiv:1412.1357.
- ¹⁶ V. Tayari, N. Hemsworth, I. Fasih, A. Favron, E. Gaufrés, G. Gervais, R. Martel, and T. Szkopek, arXiv:1412.0259.
- ¹⁷ Motohiko Ezawa, *New. J. Phys.* **16**, 115004 (2014).
- ¹⁸ Douglas R. Hofstadter, *Phys. Rev. B* **14**, 2339 (1976).
- ¹⁹ Godfrey Gumbs and Paula Fekete, *Phys. Rev. B* **56**, 3787 (1997).
- ²⁰ Tsuneya Ando and Yasutada Uemura, *J. Phys. Soc. Jpn.* **36** 959 (1974).
- ²¹ Wen Yang, Kai Chang, *Phys. Rev. B* **73** 045303 (2006).
- ²² Krstajic P. M. and Vasilopoulos P., *Phys. Rev. B* **86** 115432 (2012).
- ²³ Xiaoying Zhou, Yiman Liu, Ma Zhou, Dongsheng Tang and Guanghui Zhou, *J. Phys.: Condens. Matter* **26** 485008 (2014).
- ²⁴ Toshiya Nagahama, Michihiro Kobayashi, Yuichi Akahama, Shoichi Endo and Shin-ichiro Narita, *J. Phys. Soc. Jpn.* **54** 2096 (1985).
- ²⁵ Ruixiang Fei, Vy Tran and Li Yang, arXiv:1501.00706.